



**HAL**  
open science

# A Short-Term Negative Eddy Feedback on Midlatitude Jet Variability due to Planetary Wave Reflection

Gwendal Rivière, Loïc Robert, Francis Codron

► **To cite this version:**

Gwendal Rivière, Loïc Robert, Francis Codron. A Short-Term Negative Eddy Feedback on Midlatitude Jet Variability due to Planetary Wave Reflection. *Journal of the Atmospheric Sciences*, 2016, 73 (11), pp.4311 - 4328. 10.1175/JAS-D-16-0079.1 . hal-01401687

**HAL Id: hal-01401687**

**<https://hal.sorbonne-universite.fr/hal-01401687>**

Submitted on 23 Nov 2016

**HAL** is a multi-disciplinary open access archive for the deposit and dissemination of scientific research documents, whether they are published or not. The documents may come from teaching and research institutions in France or abroad, or from public or private research centers.

L'archive ouverte pluridisciplinaire **HAL**, est destinée au dépôt et à la diffusion de documents scientifiques de niveau recherche, publiés ou non, émanant des établissements d'enseignement et de recherche français ou étrangers, des laboratoires publics ou privés.

## A Short-Term Negative Eddy Feedback on Midlatitude Jet Variability due to Planetary Wave Reflection

GWENDAL RIVIÈRE AND LOÏC ROBERT

*Laboratoire de Météorologie Dynamique/IPSL, Ecole Normale Supérieure/CNRS/UPMC, Paris, France*

FRANCIS CODRON

*LOCEAN/IPSL, Université Pierre et Marie Curie/CNRS/IRD, Paris, France*

(Manuscript received 8 March 2016, in final form 20 June 2016)

### ABSTRACT

A three-level quasigeostrophic model on the sphere is used to identify the physical nature of the negative planetary wave feedback on midlatitude jet variability. A first approach consists of studying the nonlinear evolution of normal-mode disturbances in a baroclinic westerly zonal jet. For a low-zonal-wavenumber disturbance, successive acceleration and deceleration of the jet occur as a result of reflection of the wave on either side of the jet. The planetary wave deposits momentum in opposite ways during its poleward or equatorward propagation. In contrast, a high-zonal-wavenumber disturbance is not reflected but absorbed within the subtropical critical layer. It thus only induces poleward momentum fluxes, which accelerate the jet and shift it slightly poleward. A long-term simulation forced by a relaxation toward a zonally symmetric temperature profile is then analyzed. Planetary waves are shown to be baroclinically excited. When they propagate equatorward, they induce an acceleration of the jet together with a slight poleward shift. About two-thirds of the planetary waves are absorbed by the subtropical critical layer, which allows the accelerated poleward-shifted jet to persist for a while. For the remaining third, the potential vorticity equatorward of the jet is so well homogenized that a reflection occurs. It is followed by an abrupt jet deceleration during the subsequent poleward propagation. The reflection of planetary waves on the poleward side of the jet is more systematic because of the quasi-permanent presence of a turning latitude there. This negative planetary wave feedback is shown to act more on pulses of the jet than on its latitudinal shifts.

### 1. Introduction

Midlatitude jet variability is usually described using the leading empirical orthogonal function (EOF) of the zonally averaged zonal wind, sometimes called the zonal index (Yu and Hartmann 1993; Feldstein and Lee 1998; Gerber and Vallis 2007). This index is closely related to the leading EOF of the tropospheric geopotential height, the so-called annular mode introduced by Thompson and Wallace (2000). These modes of jet variability mainly represent latitudinal fluctuations of the jet and are triggered by variations of the eddy momentum fluxes. The same eddy momentum fluxes also act to maintain the different phases of the leading modes through a positive eddy feedback, which lasts a few

weeks after the peak of the phases (Robinson 1996, 2000; Lorenz and Hartmann 2001). As such, the positive feedback increases the persistence of the leading modes and accounts for their dominance: because it is present mainly for latitudinal shifts of the jet and much less for variations of its intensity, the eddy feedback explains why the leading mode strongly projects onto the former and much less onto the latter jet changes (Lorenz and Hartmann 2001, 2003; Barnes and Hartmann 2011).

The positive eddy feedback is primarily due to synoptic, high-frequency waves whose momentum flux convergence maintains the zonal wind anomalies even a few weeks after their peak (Feldstein and Lee 1998; Lorenz and Hartmann 2001). Several studies suggested that the efficiency of the positive eddy feedback decreases with the mean jet latitude (Kidston and Gerber 2010; Barnes and Hartmann 2010). However, there is still a debate on the exact nature of the positive synoptic eddy feedback (e.g., Robinson 2000; Lorenz and

---

Corresponding author address: Gwendal Rivière, LMD-ENS, 24 rue Lhomond, 75005 Paris, France.  
E-mail: griviere@lmd.ens.fr

Hartmann 2003; Robinson 2006; Barnes and Hartmann 2011; Zhang et al. 2012; Zurita-Gotor et al. 2014): some studies emphasize the role of barotropic mechanisms whereby a jet shift creates a change in the horizontal propagation of the waves (e.g., Barnes and Hartmann 2011; Lorenz 2014). Some others focus on baroclinic mechanisms in which the jet shift induces a change in the latitude of the baroclinicity and thus a change in the latitude of wave stirring, which in turn impacts the latitude of momentum flux convergence (e.g., Robinson 2000; Zurita-Gotor et al. 2014). Others again propose mixed barotropic–baroclinic mechanisms in which the latitude of the lower baroclinicity determines the nature of wave propagation at upper levels (Rivière 2009).

On the contrary, the planetary, low-frequency waves act to hasten the short-term decay of the zonal wind anomalies during the first week following their peak (Feldstein and Lee 1998; Watterson 2002). By analyzing observational datasets, Lorenz and Hartmann (2003) showed that the jet acts as a waveguide for these waves; so they propagate into the jet and remove momentum from it. This general behavior of planetary waves is well reproduced in simple models (O'Rourke and Vallis 2013). However, the underlying mechanisms explaining the short-term damping effect of planetary-scale waves on jet variability have not been deeply examined in the literature, and studies discussing this negative planetary eddy feedback (Lorenz and Hartmann 2003; Simpson et al. 2014) are much less numerous than for the positive synoptic eddy feedback. And yet the difficulties encountered by climate models in representing the annular mode variability might not only come from a misrepresentation of the positive synoptic feedback (Arakelian and Codron 2012; Barnes and Polvani 2013) but also from a misrepresentation of planetary waves and their negative feedback (Simpson et al. 2014). There is therefore a clear need for further investigation of the planetary wave effect on midlatitude jet variability in a more systematic manner, as done in the present paper.

The waveguide effect of westerly jets on planetary waves has been underlined by different studies (e.g., Hoskins and Ambrizzi 1993; Branstator 2002; Lorenz and Hartmann 2003). Following linear theories, such a waveguide exists when turning latitudes (or equivalently reflecting levels) exist on both sides of the jet. However, the presence of a waveguide is far from being systematic: it depends on the wavenumber and on the strength of the westerly jet. For instance, the Asian jet is more likely to act as a waveguide because it is strong and sharp enough (Hoskins and Ambrizzi 1993). Generally speaking, because of the stronger planetary vorticity gradient at lower latitudes, quasi-stationary and low-frequency

Rossby waves tend to have a turning latitude on the poleward flank of the westerly jets and a critical latitude (i.e., where the phase speed equals the background zonal wind) on the equatorward flank (Karoly 1983; Lorenz 2014). When the waves approach the critical latitude, linear theory predicts that the waves will be absorbed (Held 1983). However, when during their nonlinear stage the waves break near the critical latitude in a region called the critical layer, they feed back onto their environment and tend to homogenize the potential vorticity. This leads to a near-zero potential vorticity gradient within the critical layer, which will favor a reflection of the waves (Geisler and Dickinson 1974; Held 1983). If the critical layer is of finite extent, the nonlinear theory of Rossby wave critical layer thus predicts that the critical layer will necessarily become reflective after some time (Killworth and McIntyre 1985). This theory has been largely confirmed in realistic numerical experiments of localized Rossby wave trains propagating into the subtropics (Brunet and Haynes 1996; Magnusdottir and Haynes 1999). In observational data, one-third of planetary Rossby wave breakings occurring near a subtropical critical latitude seem to lead to reflection (Abatzoglou and Magnusdottir 2004).

Most of these wave–mean flow interaction studies focused on nonlinear processes within the critical layer itself. They did not pay attention to the later evolution of the reflecting waves and their feedback on the jet outside of the critical layer. More recently, Abatzoglou and Magnusdottir (2006) started such an analysis by comparing the effects on the North Atlantic Oscillation (NAO) of reflecting and nonreflecting planetary wave breakings occurring in the subtropical North Atlantic. Nonreflecting waves continuously induce poleward momentum fluxes when they approach the subtropics, which drive an extended positive NAO phase. On the contrary, reflecting waves first induce poleward momentum fluxes and then equatorward fluxes after their reflection, which suddenly stop the development of the positive NAO phase and even create a reversal of the polarity of the NAO a few days after the reflection. Our main purpose in this paper is to show that more generally the short-term negative feedback by planetary waves on jet variability can be attributed to reflecting waves.

We analyze the interaction of planetary waves and jet variability using a three-level quasigeostrophic model on the sphere, addressing the following questions:

- Why and in which circumstances do planetary waves reflect near the subtropical critical layer?
- How do planetary wave reflections on both sides of the jet affect the jet variability?

Section 2 presents the model, the setup of the numerical experiments, and the diagnostic tools. Section 3 analyzes the life cycles of nonlinear baroclinic disturbances having a normal-mode structure at the initial time. Then a detailed study of a long-term integration of the model forced by a relaxation to a prescribed zonally symmetric temperature profile is made in section 4. Conclusions and a discussion are presented in section 5.

## 2. Methodology

### a. Model

We use the quasigeostrophic (QG) model of Marshall and Molteni (1993, hereinafter MM93). It is a three-level spectral model on the sphere that integrates the potential vorticity (PV) equation at each vertical level  $i$ :

$$\frac{\partial q_i}{\partial t} = -J(\psi_i, q_i) - D_i + S_i, \quad (1)$$

where  $q_i$  and  $\psi_i$  denote the PV and streamfunction. Levels  $i = 1, 2$ , and 3 correspond to 200, 500, and 800 hPa, respectively. The PV can be expressed as

$$q_1 = f + \nabla^2 \psi_1 - R_1^{-2}(\psi_1 - \psi_2), \quad (2)$$

$$q_2 = f + \nabla^2 \psi_2 + R_1^{-2}(\psi_1 - \psi_2) - R_2^{-2}(\psi_2 - \psi_3), \quad (3)$$

and

$$q_3 = f + \nabla^2 \psi_3 + R_2^{-2}(\psi_2 - \psi_3), \quad (4)$$

where  $f = 2\Omega \sin\varphi$  is the Coriolis parameter ( $\Omega$  is Earth's rotation rate and  $\varphi$  is the latitude). The Rossby radii of deformation  $R_1 = 660$  km and  $R_2 = 400$  km for the 200–500-hPa layer and the 500–800-hPa layer, respectively, are set to the same values as in Rivière (2009). Each term  $D_i$  is the sum of linear operators, including a Newtonian relaxation of temperature, a linear drag at the surface (for  $i = 3$ ), and horizontal diffusion. The term  $S_i$  is the forcing term. A T42 truncation is used.

### 1) NORMAL-MODE APPROACH

The first set of simulations consists of nonlinear evolution of unstable normal modes. The basic flow is a baroclinic westerly zonal jet centered at 45°. Its meridional profile is a Gaussian function of latitude with 15° width; the peak zonal wind speeds are 45, 22.5, and 9 m s<sup>-1</sup> at levels 1, 2, and 3, respectively. Such a profile aims at representing a typical wintertime westerly jet. The sum of the dissipation and forcing terms can be written as

$$-D_1 + S_1 = -c_H \nabla^8 q'_1 + \tau_{R1}^{-1} R_1^{-2} (\psi_1 - \psi_2), \quad (5)$$

$$-D_2 + S_2 = -c_H \nabla^8 q'_2 - \tau_{R1}^{-1} R_1^{-2} (\psi_1 - \psi_2) + \tau_{R2}^{-1} R_2^{-2} (\psi_2 - \psi_3), \quad \text{and} \quad (6)$$

$$-D_3 + S_3 = -c_H \nabla^8 q'_3 - \tau_E^{-1} \nabla^2 \psi_3 - \tau_{R2}^{-1} R_2^{-2} (\psi_2 - \psi_3), \quad (7)$$

where  $q'_i$  denote the PV minus the planetary vorticity and the Ekman damping time scale  $\tau_E = 3$  days. The forcing terms  $S_i$  are zero in this section. The value of  $c_H$  is such that the damping time scale of the shorter waves at T42 truncation is 0.02 days. The relaxation time scales  $\tau_{R1} = \tau_{R2} = 25$  days are as in the formulation of MM93. After computing the normal modes with the linear model, the resulting disturbances are introduced in the nonlinear model with weak amplitudes: the perturbation PV is 20 times smaller than the basic-state PV at the initial time.

### 2) LONG-TERM RUN

The sum of the dissipation and forcing terms can here be written as

$$-D_1 + S_1 = -c_H \nabla^8 q'_1 + \tau_{R1}^{-1} R_1^{-2} (\psi_1 - \psi_2 - \tilde{\psi}_1 + \tilde{\psi}_2), \quad (8)$$

$$-D_2 + S_2 = -c_H \nabla^8 q'_2 - \tau_{R1}^{-1} R_1^{-2} (\psi_1 - \psi_2 - \tilde{\psi}_1 + \tilde{\psi}_2) + \tau_{R2}^{-1} R_2^{-2} (\psi_2 - \psi_3 - \tilde{\psi}_2 + \tilde{\psi}_3), \quad \text{and} \quad (9)$$

$$-D_3 + S_3 = -c_H \nabla^8 q'_3 - \tau_E^{-1} \nabla^2 \psi_3 - \tau_{R2}^{-1} R_2^{-2} (\psi_2 - \psi_3 - \tilde{\psi}_2 + \tilde{\psi}_3). \quad (10)$$

The forcing terms  $S_i$  are those including variables denoted with a tilde, such as  $\tilde{\psi}_1 - \tilde{\psi}_2$  and  $\tilde{\psi}_2 - \tilde{\psi}_3$  which are proportional to the temperature-restoration field between levels 1 and 2 and between levels 2 and 3, respectively. The diffusion and dissipation coefficients  $c_H$  and  $\tau_E$  have the same values as in the normal-mode approach. The temperature relaxation coefficients are equal to  $\tau_{R1} = 40$  days and  $\tau_{R2} = 15$  days in order to get relaxation time scales similar to Held and Suarez (1994)'s framework with shorter time scales at lower levels. The restoration temperature is an error function of latitude in thermal wind balance with the zonal jet given by

$$\tilde{u}_i = U_{0i} \exp \left[ - \left( \frac{\varphi - \varphi_0}{d\varphi} \right)^2 \right]. \quad (11)$$

The jet latitude is  $\varphi_0 = 30^\circ\text{N}$ , its width  $d\varphi = 20^\circ$ , and the velocity at the different levels  $U_{01} = 50$  m s<sup>-1</sup>,  $U_{02} = 25$  m s<sup>-1</sup>, and  $U_{03} = 10$  m s<sup>-1</sup>. The simulation lasts

15 years; the first 300 days have been removed before the analysis.

### b. Refractive index

The refractive index of waves within the three-level quasigeostrophic framework on the sphere can be expressed as (see [appendix](#))

$$n_1^2 = \frac{\partial \bar{q}_1 / \partial y}{\bar{u}_1 - ca \cos \varphi} - \frac{R_2^2}{R_1^2} \left( \frac{1}{R_1} - \frac{1}{R_2} \right)^2 - \frac{m^2}{a^2 \cos^2 \varphi}, \quad (12)$$

$$n_2^2 = \frac{\partial \bar{q}_2 / \partial y}{\bar{u}_2 - ca \cos \varphi} - \left( \frac{1}{R_1} - \frac{1}{R_2} \right)^2 - \frac{m^2}{a^2 \cos^2 \varphi}, \quad \text{and} \quad (13)$$

$$n_3^2 = \frac{\partial \bar{q}_3 / \partial y}{\bar{u}_3 - ca \cos \varphi} - \frac{R_1^2}{R_2^2} \left( \frac{1}{R_1} - \frac{1}{R_2} \right)^2 - \frac{m^2}{a^2 \cos^2 \varphi}, \quad (14)$$

where  $\bar{u}$  and  $\bar{q}$  are the zonal-mean zonal wind and PV, respectively;  $c$  is the angular phase speed of the disturbance,  $a$  is Earth's radius, and  $m$  is the nondimensional zonal wavenumber. The second terms on the rhs of Eqs. (12), (13), and (14) take into account the variations of the stratification with height, similarly to the continuous formulation obtained in [Charney and Drazin \(1961\)](#) and [Matsuno \(1970\)](#).

In all simulations, the phase speed of waves has been computed for each day as follows: first, the meridional wind is decomposed into contributions from individual zonal wavenumbers  $m$

$$v_m(\lambda, \varphi, z, t) = A_m \cos(m\lambda + \phi_m),$$

where  $\lambda$  is longitude. By multiplying  $v_m$  by  $\cos(m\lambda)$  and  $\sin(m\lambda)$  and then zonally averaging, one obtains

$$\overline{v_m \cos(m\lambda)} = \frac{A_m}{2} \cos \phi_m \quad \text{and}$$

$$\overline{v_m \sin(m\lambda)} = -\frac{A_m}{2} \sin \phi_m.$$

The phase  $\phi_m$  is thus given by the angle of the previous vector. The difference of  $\phi_m$  between day  $d$  and its successor  $d + 1$  is then computed to get an estimation of the angular phase speed  $c$  of the waves present at each day  $d$ .

### 3. Normal-mode study

The nonlinear evolution of unstable baroclinic normal modes for individual zonal wavenumbers  $m \in [3, 11]$  is analyzed in the present section. While such an approach has been intensively adopted since the 1970s ([Gall 1976](#); [Simmons and Hoskins 1978](#)), the following results, which focus on the successive stages of the

nonlinear evolution and the difference between planetary and synoptic waves, do not seem to have been underlined before. For our basic flow, the most unstable wavenumbers are  $m = 6, 7,$  and  $8,$  with  $e$ -folding times equal to 1.9, 1.8, and 1.9 days, respectively. Since the disturbances have small initial amplitudes, a few days are needed for them to reach finite amplitudes. The jet begins to be visibly modified around  $t = 4$  days, roughly at the same time as when the momentum flux convergence reaches strong values (see [Fig. 1](#)).

Normal-mode disturbances have a pronounced anticyclonic tilt because of spherical geometry ([Simmons and Hoskins 1978](#); [Balasubramanian and Garner 1997](#)). Indeed, the stronger planetary vorticity gradient on the equatorward side of the jet also makes the refractive index stronger there than on the poleward side, as seen in Eqs. (12)–(14) ([Rivi re 2009](#)). This leads to predominant poleward momentum fluxes during the first stage of the nonlinear evolution of the normal modes between  $t = 4$  and 8 days. Hence, a dipolar structure in the momentum flux convergence appears during that time interval, with positive and negative values on the poleward and equatorward sides of the jet, respectively. The jet moves poleward and accelerates, as can be clearly seen at  $t = 8$  days for the most unstable wavenumbers ( $m \in [5, 8]$ ). Note also that the jet becomes narrower at  $t = 8$  days than at  $t = 0$  days.

After this first stage of the nonlinear evolution, the behavior of the disturbances and their feedback onto the jet vary depending on their wavenumber. For low wavenumbers ( $m \in [4, 6]$ ), as soon as the jet is accelerated, the momentum flux convergence abruptly reverses sign with negative values on the jet core and on its poleward flank and positive values on its equatorward flank. This occurs between  $t = 11$  and 14 days for  $m = 4$  ([Fig. 1a](#)) and between  $t = 8$  and 11 days for  $m = 5$  and 6 ([Figs. 1b,c](#)). This sign reversal of the momentum flux convergence leads to a decelerated jet with a minimum intensity reached at  $t = 16, 12,$  and 11 days for  $m = 4, 5,$  and 6, respectively. After this second stage, yet another sign reversal of the momentum flux convergence is observed, which creates a new acceleration of the jet. This alternation in the sign of the momentum flux convergence continues with decreasing amplitudes until  $t = 20$  days.

For higher wavenumbers ( $m \in [7, 9]$ ), the alternation in the sign of the momentum flux convergence barely occurs ([Figs. 1d–f](#)). After a nonlinear stage during which synoptic disturbances mainly accelerate the jet, the jet intensity slowly decreases with time because of the dissipating processes.

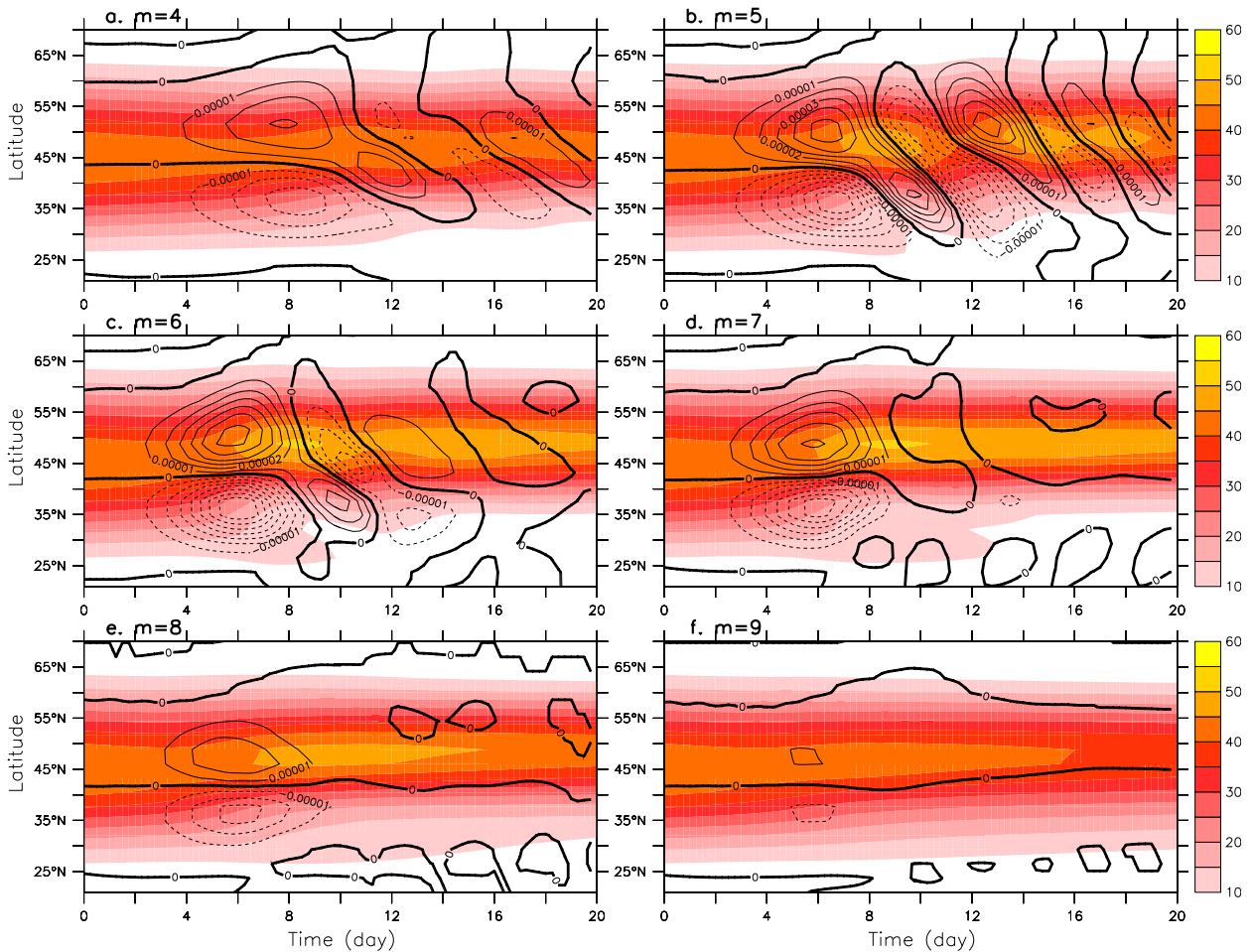


FIG. 1. Zonally averaged zonal wind (shadings;  $\text{m s}^{-1}$ ) and momentum flux convergence [contours; contour interval (CI):  $10^{-5} \text{ m s}^{-2}$ ] at 200 hPa as a function of time for nonlinear simulations of unstable normal modes with zonal wavenumbers  $m =$  (a) 4, (b) 5, (c) 6, (d) 7, (e) 8, and (f) 9.

Figure 2 summarizes the behavior of disturbances of different wavenumbers by projecting the momentum flux convergence at each time on the momentum flux convergence at the initial time:

$$P(t) = \sum_y [u^*v^*](y, t) \frac{[u^*v^*](y, 0)}{\sqrt{\sum_y [u^*v^*](y, 0)^2}}, \quad (15)$$

where asterisks denote the deviation from the zonal mean and square brackets denote the zonal mean. Wavenumbers that induce the strongest signal at the beginning of the first nonlinear stage ( $t = 4$  days) are  $m = 6, 7,$  and  $8$ , which makes sense since they are the most unstable wavenumbers. For  $m \in [4, 6]$ , the projections oscillate between positive and negative values. These oscillations are still slightly visible for  $m = 7$ . On the contrary, for  $m \in [8, 10]$ , the projections smoothly decrease toward zero after reaching their peak.

To better understand this oscillatory behavior of the momentum flux convergence for low wavenumbers, we analyze the structural changes of the disturbances. We focus on wavenumber  $m = 5$  because it is the clearest case. Figure 3a shows the normal mode initialized in the nonlinear model. The disturbance mainly tilts anticyclonically across the jet core, leading to positive and negative momentum flux convergence to the north and south, respectively. At  $t = 7$  days (Fig. 3b), the disturbance has less meridional extent but is still anticyclonically tilted. Its amplitude also peaks at a lower latitude than at the initial time. At  $t = 10$  days (Fig. 3c), the structure of the disturbance suddenly changes and becomes marked by a pronounced cyclonic tilt. At that time, the amplitude peaks within the latitudinal band  $[45^\circ, 50^\circ\text{N}]$  while before ( $t = 7$  days) it was more within  $[40^\circ, 45^\circ\text{N}]$ . Finally at  $t = 13$  days, the disturbance tilts anticyclonically again. These successive changes in the

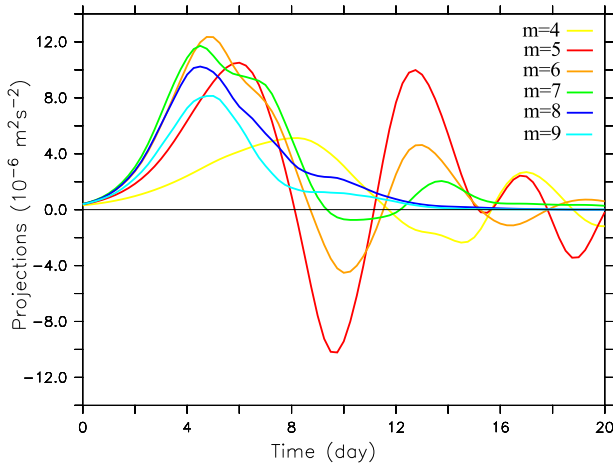


FIG. 2. Projection  $P(t)$  [see Eq. (15)] of the vertically-averaged momentum flux convergence at any time on the vertically averaged momentum flux convergence at the initial time for nonlinear simulations of normal modes with different zonal wavenumbers.

tilt of the wave show that there are reflections on both sides of the jet. First, between  $t = 0$  and 7 days, the wave propagates toward lower latitudes and is reflected on the equatorward side of the jet between  $t = 7$  and 10 days. Then the wave propagates poleward with a new reflection occurring on the poleward flank of the jet between  $t = 10$  and 13 days.

Computing the refractive index at different times confirms the existence of a waveguide effect for low

wavenumbers only (Fig. 4). Before the first stage of jet acceleration ( $t = 6$  days), the  $m = 5$  perturbation has a turning latitude on the poleward flank of the jet near  $55^\circ\text{N}$  and a critical latitude on its equatorward flank near  $33^\circ\text{N}$  (Figs. 4a,c). At  $t = 8$  days, the jet is accelerated and is sharper than previously. In particular, we note a strong decrease of the zonal wind near  $35^\circ\text{N}$  leading to an important change in the curvature of the jet profile. This gives a significant decrease in potential vorticity gradient between the jet core and the critical latitude. The consequence is a rapid decrease in the refractive index toward zero, reached near  $37^\circ\text{N}$ . Therefore, the wave meets a turning latitude before its critical latitude and is reflected poleward. The formation of a temporary turning latitude is not only due to the decrease in potential vorticity gradient but also to the fact that the critical layer does not shift poleward when the westerlies decrease on the equatorward side of the jet (Fig. 4a). This is the decrease in phase speed during the equatorward wave propagation that roughly maintains the critical layer at the same place. The turning latitude still exists at  $t = 10$  days when the jet remains intense and sharp but then disappears at  $t = 12$  days because the wave propagates poleward after the reflection, which acts to broaden the jet and to suppress the turning latitude (Figs. 4a,c).

High wavenumbers do not create temporary turning latitudes on the equatorward flank of the jet even when it has accelerated and becomes sharper, as seen in the

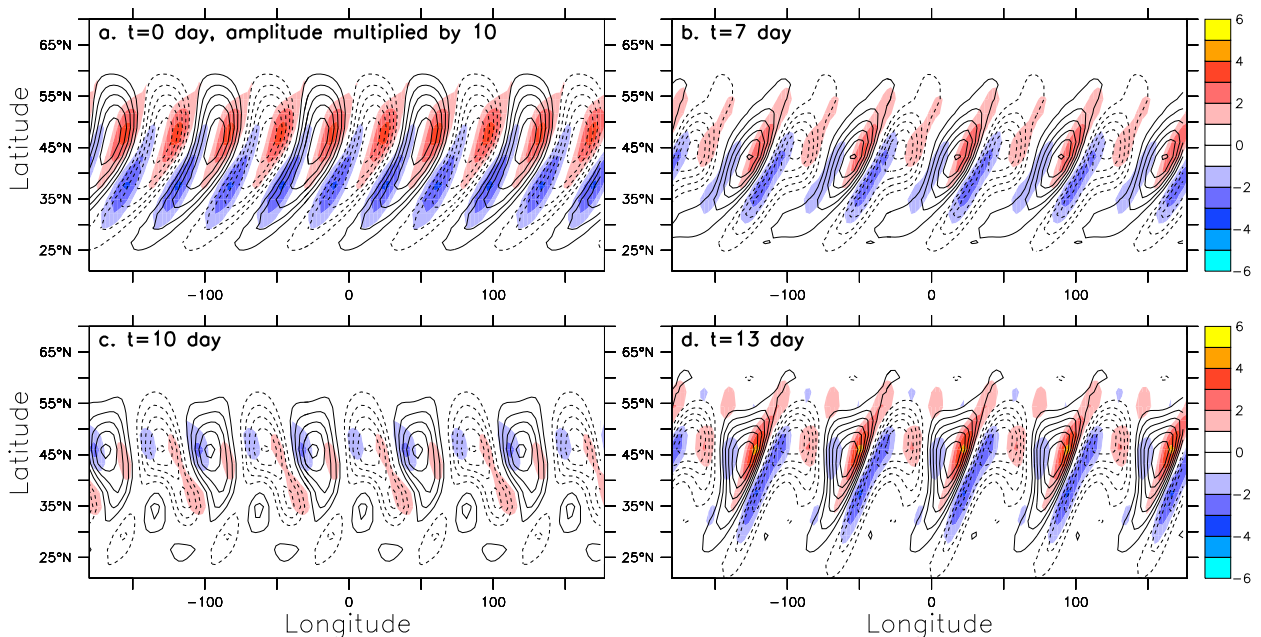


FIG. 3. Anomalous relative vorticity (contours;  $8 \times 10^{-6} \text{ s}^{-1}$ ) and momentum flux convergence (shadings;  $10^{-4} \text{ m s}^{-2}$ ) at 200 hPa for the nonlinear simulation of the unstable normal mode with  $m = 5$  at  $t =$  (a) 0 (b) 7, (c) 10, and (d) 13 days.

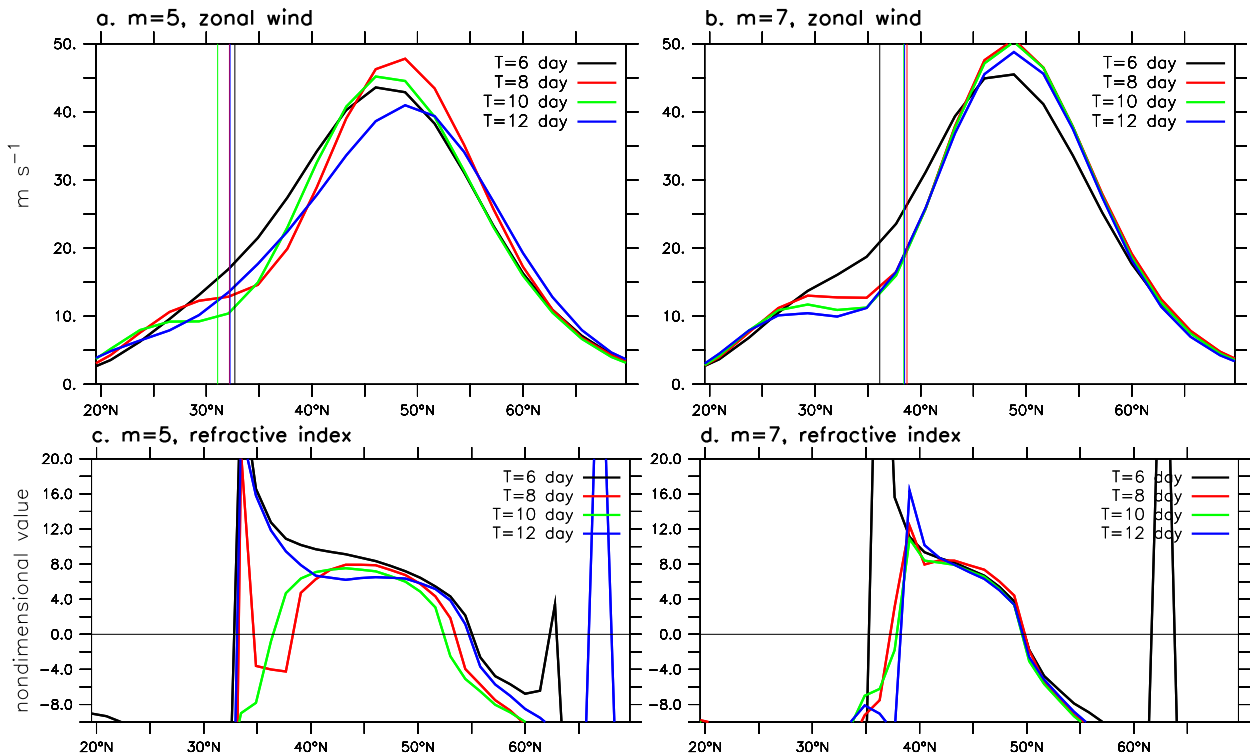


FIG. 4. (top) Zonally averaged zonal wind at 200 hPa for the nonlinear simulations of unstable normal modes with  $m =$  (a) 5 and (b) 7. The vertical lines correspond to the critical latitudes of the days of interest. (bottom) Nondimensional refractive index  $a/n|\text{sign}(n^2)$  at 200 hPa for  $m =$  (c) 5 and (d) 7.

$m = 7$  case (Figs. 4b,d): the refractive index in fact increases until the critical latitude. In contrast with the  $m = 5$  case, the critical layer shifts poleward (Fig. 4b) when the jet sharpens because the zonal winds decrease and the phase speed does not change. Therefore, the decrease in potential vorticity gradient during the sharpening of the jet is necessary to make a turning latitude appear but is not enough to completely explain its occurrence. A reduction in phase speed as seen for  $m = 5$  and not for  $m = 7$  is an additional important factor for the formation of a transient turning latitude on the equatorward side of the jet.

To summarize, during their nonlinear evolution, planetary waves drive a succession of acceleration and deceleration of the jet because they tend to reflect on both sides of the jet and deposit their momentum in opposite regions during their poleward and equatorward propagation within the waveguide. The turning latitude on the poleward side is always present, while that on the equatorward side is transient and depends on the ability of the waves to reduce the potential vorticity gradient during their equatorward propagation toward the critical layer. Therefore, planetary waves can force variations of the jet that are quickly

suppressed by the same waves once they are reflected. The latter effect will appear as a negative feedback of planetary waves on changes of the jet. On the contrary, synoptic waves only force a single acceleration of the jet because they are absorbed within the critical layer and not reflected. It is important to note that the transition wavenumber between reflection and absorption depends on the basic flow properties. In the next section, the transition wavenumber will be different, and the separation between synoptic and planetary waves will differ.

#### 4. Long-term simulation

The long-term simulation will serve to confirm the previous results when all wavenumbers interact with each other.

##### a. Model climatology

While the forcing latitude is  $\varphi_0 = 30^\circ\text{N}$ , the mean position of the jet is around  $45^\circ\text{N}$  (dashed curve in Fig. 5). Such a difference is due to the dominance of anticyclonic wave breaking in the model, which tends to deposit momentum on the poleward side of the

excitation zone (Rivière 2009). The latitudinal distributions of the time-mean momentum flux convergence and heat fluxes for various wavenumbers are also shown in Fig. 5. The patterns vary strongly from wavenumber to wavenumber. For  $m = 3$ , heat fluxes reach their maximum on the poleward side of the jet near  $55^\circ\text{N}$ , while the momentum flux convergence peaks closer to  $60^\circ\text{N}$ . This slight shift can be attributed to the spherical geometry since waves tend to tilt anticyclonically and deposit their momentum poleward of the heat fluxes (Rivière 2009). In contrast to the  $m = 3$  case, heat fluxes for  $m = 4$  have larger amplitude on the equatorward side of the jet. The momentum flux convergence peaks at two distinct latitudes: one on the equatorward side of the jet near the heat flux maximum, and another one on the poleward side near  $55^\circ\text{N}$ . The latter peak may seem surprising; it is not associated with a peak in heat fluxes and cannot be attributed to barotropic instability either since the PV gradient at the upper level does not change sign in this particular region. For  $m = 5$ , the maximum in heat fluxes is on the equatorward side of the jet as for  $m = 4$ , but the momentum flux convergence has a single poleward-shifted maximum as for  $m = 3$ . For  $m = 6$  and 7, the heat fluxes and the momentum flux convergence both peak close to the jet core. The higher phase speeds of these synoptic waves make their low-level critical layer occur closer to the jet core, and baroclinic instability is more likely in that region than for planetary waves (Zhang et al. 2012).

To summarize, the model shows some classical features of this type of model (Zhang et al. 2012; O'Rourke and Vallis 2013), such as the deposition of momentum on the jet flanks by planetary waves and on the jet core by synoptic waves. The distribution of eddy momentum fluxes is mainly explained by baroclinic instability, as in Zhang et al. (2012), and not by barotropic instability (O'Rourke and Vallis 2013). Indeed, there is a general one-to-one correspondence between the lower-level heat fluxes and the momentum flux convergence, with a slight shift due to spherical geometry. One exception is the second peak of momentum flux convergence for  $m = 4$  on the poleward side of the jet, which is not linked to a peak in heat fluxes and will be shown to be a signature of a waveguide effect in next sections.

### b. Snapshots

In the rest of the paper, planetary waves will mean wavenumbers  $m \in [1, 4]$  and synoptic waves  $m \in [5, 8]$ . They were separated according to the climatological patterns of momentum flux convergence of Fig. 5, which peak outside the jet core for  $m \in [1, 4]$  and inside it for

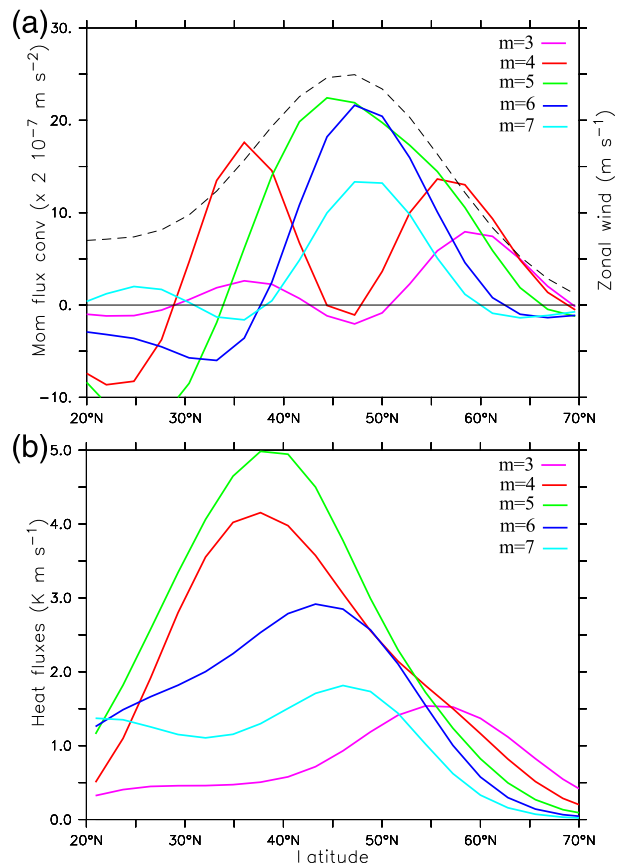


FIG. 5. Model climatology of (a) the vertically averaged momentum flux convergence for different wavenumbers (solid lines) and the vertically averaged zonal wind (dashed line) and (b) the heat flux at the interface between the two lowest levels for the long-term simulation.

$m \in [5, 8]$ . Waves with wavenumbers greater than 8 have very weak amplitudes, and are not considered in what follows.

To demonstrate the role of planetary waves, we first focus on a 20-day interval of the simulation during which the jet strongly fluctuates in amplitude (Fig. 6). Long waves exhibit an alternation of poleward and equatorward momentum fluxes, with the former having greater amplitude (Fig. 6a). Since the meridional group velocity and the meridional momentum fluxes have opposite sign for Rossby waves (see Vallis 2006, p. 490), the figure shows an alternation of poleward and equatorward propagation of planetary wave energy. Hence, a waveguide effect is operating on the equatorward flank of the jet, as seen in the peak amplitudes, which are more often reached on the equatorward flank than in the jet core. The alternation in the orientation of propagation of planetary waves creates an alternation in the sign of the momentum

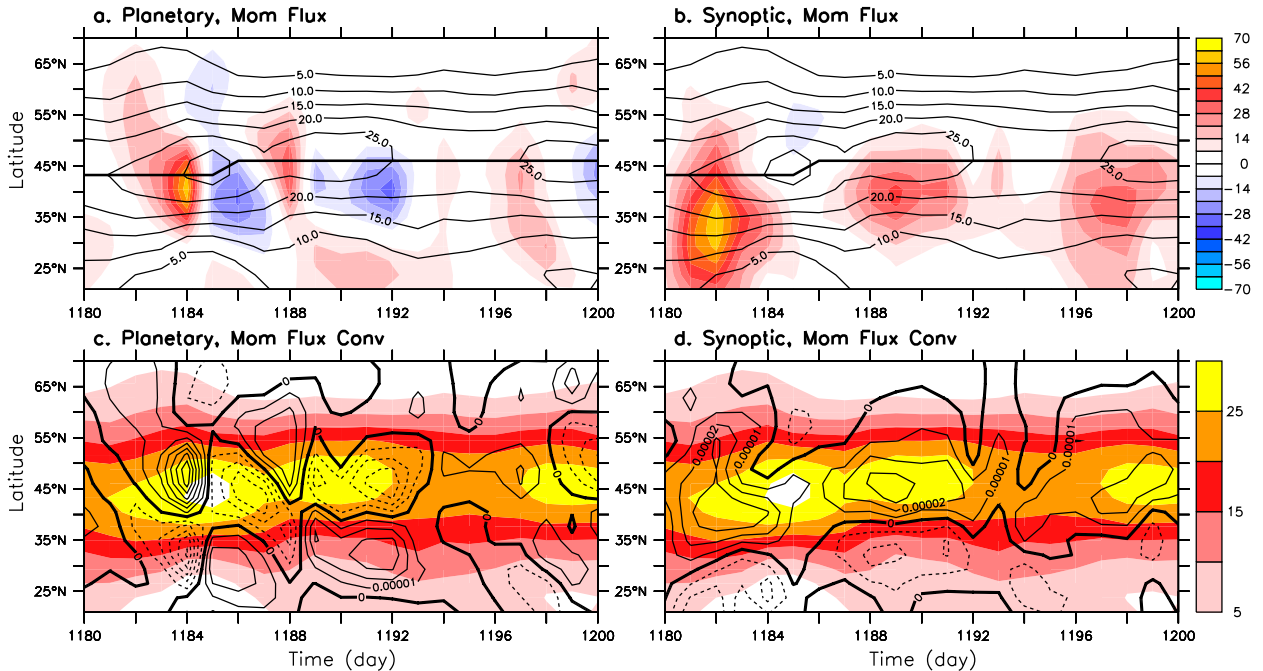


FIG. 6. (top) Vertically averaged momentum flux (shadings;  $\text{m}^2 \text{s}^{-2}$ ) and zonal wind (contours;  $\text{CI: } 5 \text{ m s}^{-1}$ ) as a function of time and latitude from  $t = 1180$  to 1200 days of the long-term simulation. (bottom) Vertically averaged momentum flux convergence (contours;  $\text{CI: } 10^{-5} \text{ m s}^{-2}$ ) and zonal wind (shadings;  $\text{m s}^{-1}$ ) as a function of time and latitude. (a),(c) Planetary wave and (b),(d) synoptic wave.

flux convergence (Fig. 6c). During their equatorward propagation, planetary waves induce poleward momentum fluxes leading to positive and negative momentum flux convergence in the jet core and equatorward of it, respectively (see  $t = 1184$ , 1188, and 1197 days). On the contrary, during the poleward propagation of planetary waves, the associated momentum flux convergence is negative in the jet core and positive equatorward of it (see  $t = 1186$ , 1191, and 1200 days).

Synoptic waves only produce poleward momentum fluxes with peak amplitudes on the equatorward flank of the jet, leading to convergence of the momentum fluxes in the jet core (see Fig. 6b from  $t = 1180$  to 1184 days, from  $t = 1188$  to 1192 days, and from  $t = 1196$  to 1200 days). In more rare cases somewhat outside of the jet core (not shown). This behavior is consistent with the climatology of momentum flux convergence shown in Fig. 5a.

Even though the separation between synoptic and planetary waves is based on the climatological patterns of the momentum flux convergence, we observe that it corresponds well to a separation between reflecting and non-reflecting waves. We have checked that  $m = 4$  exhibits an alternation of poleward and equatorward momentum fluxes, whereas  $m = 5$  shows poleward momentum fluxes only.

The previously described fluctuations of the eddy momentum flux convergence force changes in the jet intensity (Figs. 6c,d). The first peak in jet intensity at  $t = 1185$  days is forced by both synoptic and planetary waves during the preceding days. Even though synoptic waves act to maintain the jet intensity during and after that peak, the jet is decelerated between  $t = 1185$  and 1192 days by planetary waves (Figs. 6c,d). Another acceleration of the jet occurs between  $t = 1197$  and 1200 days and is also forced by both synoptic and planetary waves, and its deceleration is due to negative momentum flux convergence induced by planetary waves near  $t = 1203$  (not shown).

We now focus on the first intense phase of the jet around  $t = 1184$  days and on wavenumber  $m = 4$  that dominates the strong negative feedback. Figure 7 shows the  $m = 4$  meridional wind and its associated momentum flux convergence on different days. The wave changes its structure rapidly with time. At  $t = 1183$  days (Fig. 7a), the wave is meridionally tilted over a broad latitudinal range ( $35^\circ$ – $60^\circ\text{N}$ ), with peak amplitudes in the band  $45^\circ$ – $50^\circ\text{N}$ . At  $t = 1184$  days (Fig. 7b), the wave is now tilted anticyclonically and peaks at a lower latitude near  $40^\circ\text{N}$ . This leads to positive momentum flux convergence near  $45^\circ\text{N}$  that accelerates the jet in its core region and negative momentum flux convergence near

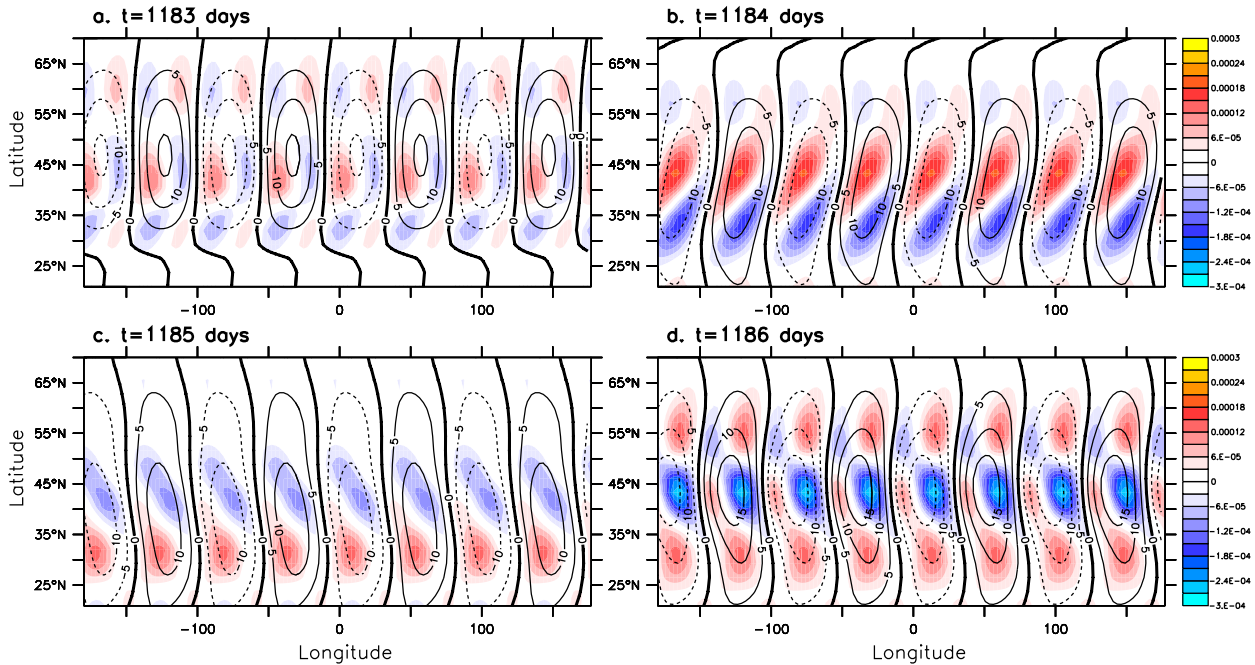


FIG. 7. Meridional wind (contours; CI:  $5 \text{ m s}^{-1}$ ) and momentum flux convergence (shadings;  $\text{m s}^{-2}$ ) at 200 hPa for zonal wavenumber  $m = 4$  at  $t =$  (a) 1183, (b) 1184, (c) 1185, and (d) 1186 days of the long-term simulation.

$35^\circ\text{N}$  that decelerates the zonal winds on the equatorward flank of the jet. On the contrary, one day later, at  $t = 1185$  days (Fig. 7c), the wave tilt is cyclonic, and the momentum flux convergence is negative near the jet core in the band  $40^\circ\text{--}45^\circ\text{N}$  and positive on its equatorward flank in the band  $30^\circ\text{--}35^\circ\text{N}$ . The strong deceleration of the jet induced by the  $m = 4$  wave is still present at  $t = 1186$  days (Fig. 7d). The peak amplitude of the wave is farther north than on the previous day. The rapid change in the wave momentum forcing of the jet thus occurs precisely at the time of the wave reflection near  $t = 1185$  days.

Figure 8 shows the vertical cross sections of the zonal wind and of the refractive index for  $m = 4$  at  $t = 1183$ , 1184, 1185, and 1186 days. A turning latitude on the equatorward flank of the jet appears at  $t = 1184$  and 1185 days, when the zonal wind on the equatorward flank of the jet is weakest. All the other cases show a positive refractive index and an increase in the refractive index as latitude decreases and therefore an absorbing critical layer. A decomposition of the factors explaining this rapid change in the refractive index is shown in Fig. 9. From  $t = 1183$  to 1184 days, when the wave propagates equatorward, the zonal wind decreases from  $20$  to  $14 \text{ m s}^{-1}$  at  $30^\circ\text{N}$  (Fig. 9b), while the PV gradient decreases from  $4 \times 10^{-11} \text{ m}^{-1} \text{ s}^{-1}$  to  $1 \times 10^{-11} \text{ m}^{-1} \text{ s}^{-1}$ . The decrease in the PV gradient dominates over that in zonal wind. It makes the ratio

$a^2(\partial\bar{q}/\partial y)/(\bar{u} - c_0 a \cos\phi)$  decrease by up to a factor of 2 between  $t = 1184$  and 1185 days (Fig. 9c), where  $c_0$  is the phase speed taken at  $t = 1184$  days. The decrease in phase speed during the equatorward propagation of the wave also participates in the low refractive index, albeit less importantly, since the differences between the ratios  $a^2(\partial\bar{q}/\partial y)/(\bar{u} - ca \cos\phi)$  at  $t = 1184$  and 1185 days are larger than the differences between the ratios  $a^2(\partial\bar{q}/\partial y)/(\bar{u} - c_0 a \cos\phi)$  (Figs. 9c,d). Such a change in the refractive index has not been detected for synoptic waves. For the latter waves, the refractive index increases as latitude decreases toward the critical layer.

To summarize, this section showed that both planetary waves and synoptic waves can drive an acceleration of the jet. In addition, synoptic waves tend to extend its duration, while planetary waves tend to suppress it. This confirms a well-known picture found in many studies (e.g., Feldstein and Lee 1998; Watterson 2002; Lorenz and Hartmann 2001). The new result of the present study is that this negative feedback from planetary waves on the jet acceleration occurs when they reflect on its equatorward flank. Similarly, the planetary waves induce a negative feedback on a jet deceleration just after their reflection on its poleward flank (see  $t = 1186$  days in Figs. 6a,c). Our results provide an interpretation for the rapid change of sign in the planetary wave momentum forcing on the leading modes of variability, as shown in Lorenz and Hartmann

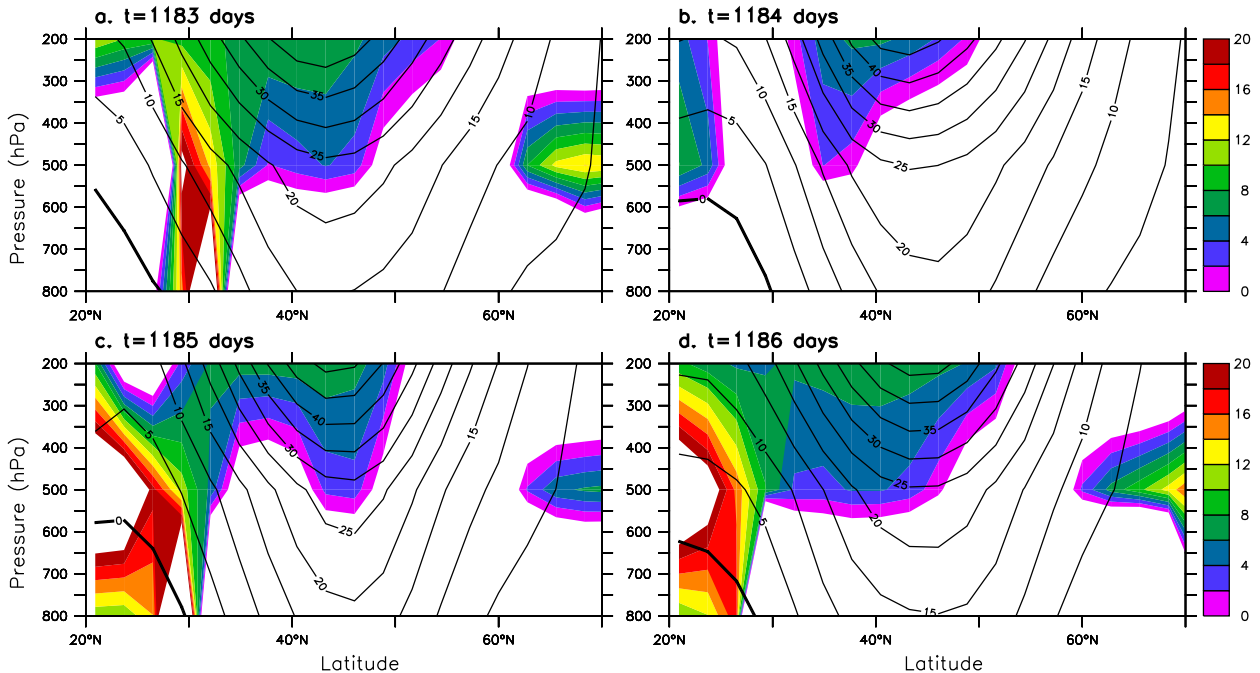


FIG. 8. Vertical cross section of the nondimensional refractive index  $a|n|\text{sign}(n^2)$  for  $m = 4$  at  $t =$  (a) 1183, (b) 1184, (c) 1185, and (d) 1186 days of the long-term simulation.

(2003) and Simpson et al. (2014). The regression of the planetary wave momentum forcing on the two first principal components is usually strongly positive 2–3 days prior to the event and strongly negative 2–3 days after the event [see, e.g., Fig. 8a of Lorenz and Hartmann (2003) or Fig. 5c of Simpson et al. (2014)]. These are the same time scales found in the present model and correspond to the time scales needed for a planetary wave to propagate from one side to another of the waveguide.

### c. Composites

The purpose of the present section is to get a more statistical point of view of the planetary wave reflection and its effect on the jet variability. A normalized index is built by averaging the planetary wave momentum fluxes over the midlatitude band (30°–60°N) and the three vertical levels. Two composites are computed based on days for which this planetary wave momentum–flux index is greater than 1.5 times its standard deviation and lower than  $-1.5$  times its standard deviation. They correspond to an equatorward and a poleward propagation of strong-amplitude planetary waves and are hereinafter denoted as Eq and Po composites, respectively. A third composite is computed for days belonging to Eq that are then followed 3 or 4 days later by a value of the index lower than  $-1.0$  standard deviation. It corresponds to reflecting periods in the subtropical regions during

which an equatorward propagation is followed by a poleward propagation a few days later. This composite is hereinafter denoted as EqPo. Eq, Po, and EqPo composites are composed of 230, 184, and 83 days of the 5175 days of the simulation.

The latitudinal structure at different lags of the momentum fluxes associated with the three composites is shown in Figs. 10 and 11. By construction, the zero-lag day for Eq corresponds to a peak in poleward momentum fluxes around 45°N (Fig. 10a). One day before, it is preceded by a peak in poleward momentum fluxes at 50°N associated with momentum flux convergence near 55°N (Fig. 10b) similar to the peak in the  $m = 4$  climatology shown in Fig. 5a. At lags  $-3$  and  $-2$  days, momentum fluxes are slightly negative, suggesting that some part of the wave energy has been reflected on the poleward side of the jet between lag  $-2$  and lag  $-1$  days. At lag  $+1$  day, there is a peak in poleward momentum fluxes around 35°N equatorward of the one at zero lag. From lag  $+2$  to lag  $+4$  days, the peak stays near 30°N. This displacement of the peak toward lower latitudes and the absence of sign reversal of the fluxes at positive lags suggest an equatorward propagation of the wave and absorption by the subtropical critical layer. Therefore, Eq composites confirm the existence of a recurrent reflection on the poleward side of the jet and show that reflection on the equatorward side occurs much less often. It also provides a dynamical

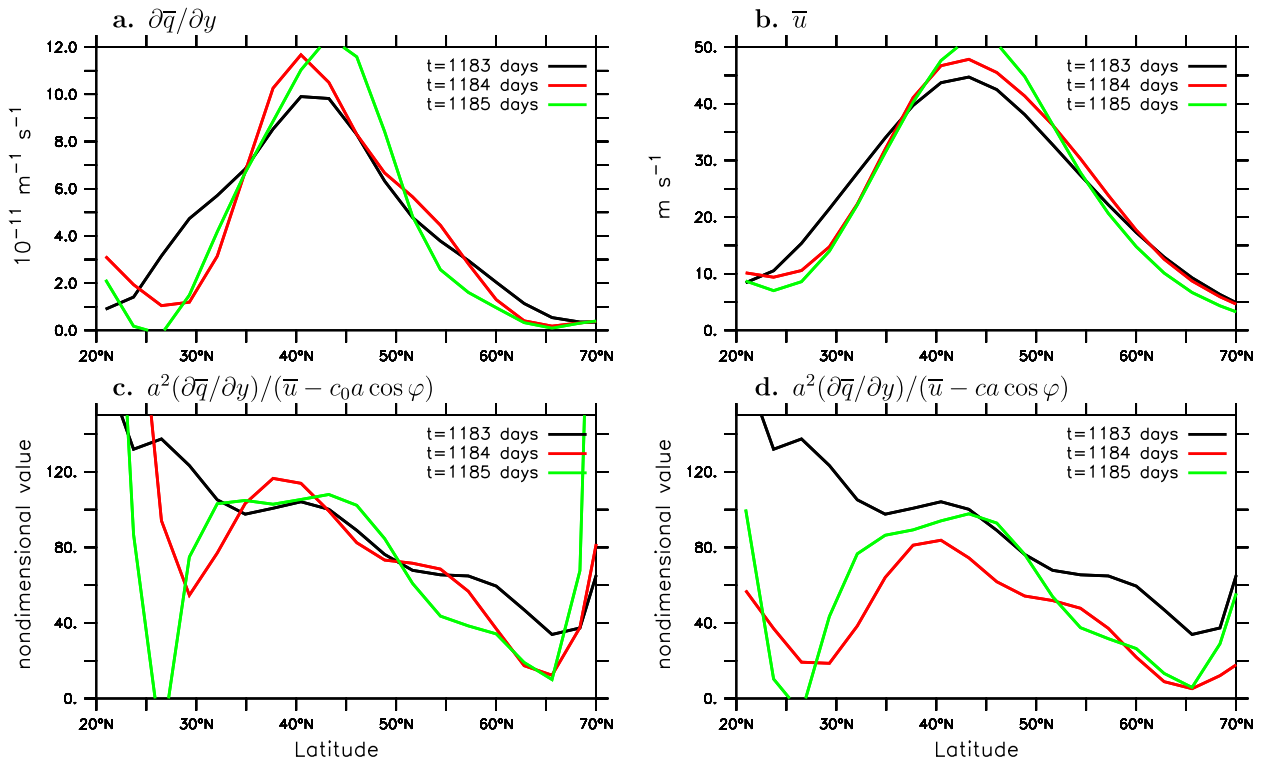


FIG. 9. Zonal averages at 200 hPa of (a) the potential vorticity gradient  $\partial\bar{q}/\partial y$ ; (b) the zonal wind  $\bar{u}$ ; (c) the ratio  $a^2(\partial\bar{q}/\partial y)/(\bar{u} - c_0 a \cos \varphi)$ , where  $c_0 = c(t = 1183 \text{ days})$  is the phase speed computed at the beginning of the period; and (d) the ratio  $a^2(\partial\bar{q}/\partial y)/(\bar{u} - ca \cos \varphi)$  for  $m = 4$ .

interpretation for the poleward peak in the climatology of the  $m = 4$  momentum flux convergence that seems to be due to wave reflection on the poleward side of the jet.

At zero-lag day, the Po composite shows a peak in equatorward momentum fluxes (Fig. 10c). This poleward propagation is preceded by an equatorward propagation at lag  $-3$  and lag  $-2$  days and is followed by an equatorward propagation from lag  $+2$  to lag  $+4$  days. This composite reflects the existence of reflection on both sides of the jet. Note that the maximum of momentum flux convergence between  $55^\circ$  and  $60^\circ\text{N}$  at lag  $+2$  days occurs just after the wave reflection on the poleward side (Fig. 10d), similar to lag  $-1$  days in the Eq composite.

The EqPo composite is built to select reflecting cases in the subtropical critical layer. It contains 83 cases, which correspond to one-third of the Eq cases, consistent with the observational study of Abatzoglou and Magnusdottir (2004).

To investigate how planetary waves and their reflection affect the nature of the jet variability, two additional normalized indices have been defined based on the daily time series of the jet latitude (hereinafter called shifting mode) and the maximum speed of the jet (hereinafter called pulsing mode), as in Barnes and Hartmann (2011). The standard deviations of these two time series are  $1.5^\circ$

and  $2.1 \text{ m s}^{-1}$ , respectively. The jet is here defined as the vertically averaged zonal-mean zonal wind.

Figure 11 shows the average evolution of the zonal wind and the shifting and pulsing indices around the days defined by the Eq, Po, or EqPo wave-based composites. For Eq, there is a rapid acceleration of the jet from lag  $-1$  to lag  $+2$  days of about  $3 \text{ m s}^{-1}$ , accompanied by a slight poleward shift of a few degrees (Fig. 11a). The pulsing index increases from  $-0.7$  to  $0.1$  during the same period, while the shifting index increases from  $-0.4$  to  $0.1$  (Fig. 11b). Then the two indices slowly decrease to zero from lag  $+2$  to lag  $+5$  days. The slightly stronger variations of the pulsing index compared to the shifting index suggest that planetary wave activity is more able to excite the pulsing mode than the shifting mode. This could be because the latitudinal band in which the waves propagate, or in other words the waveguide position, is shifted equatorward compared to the jet core (see Figs. 6a,b). Indeed, if the waveguide was symmetric with respect to the mean jet axis, the deposit of momentum would occur on both flanks of the jet depending on the orientation of the wave. This would facilitate the triggering of the shifting mode. Since the waveguide is displaced equatorward, an equatorward-propagating wave tends to deposit momentum on the jet core and accelerate the jet.

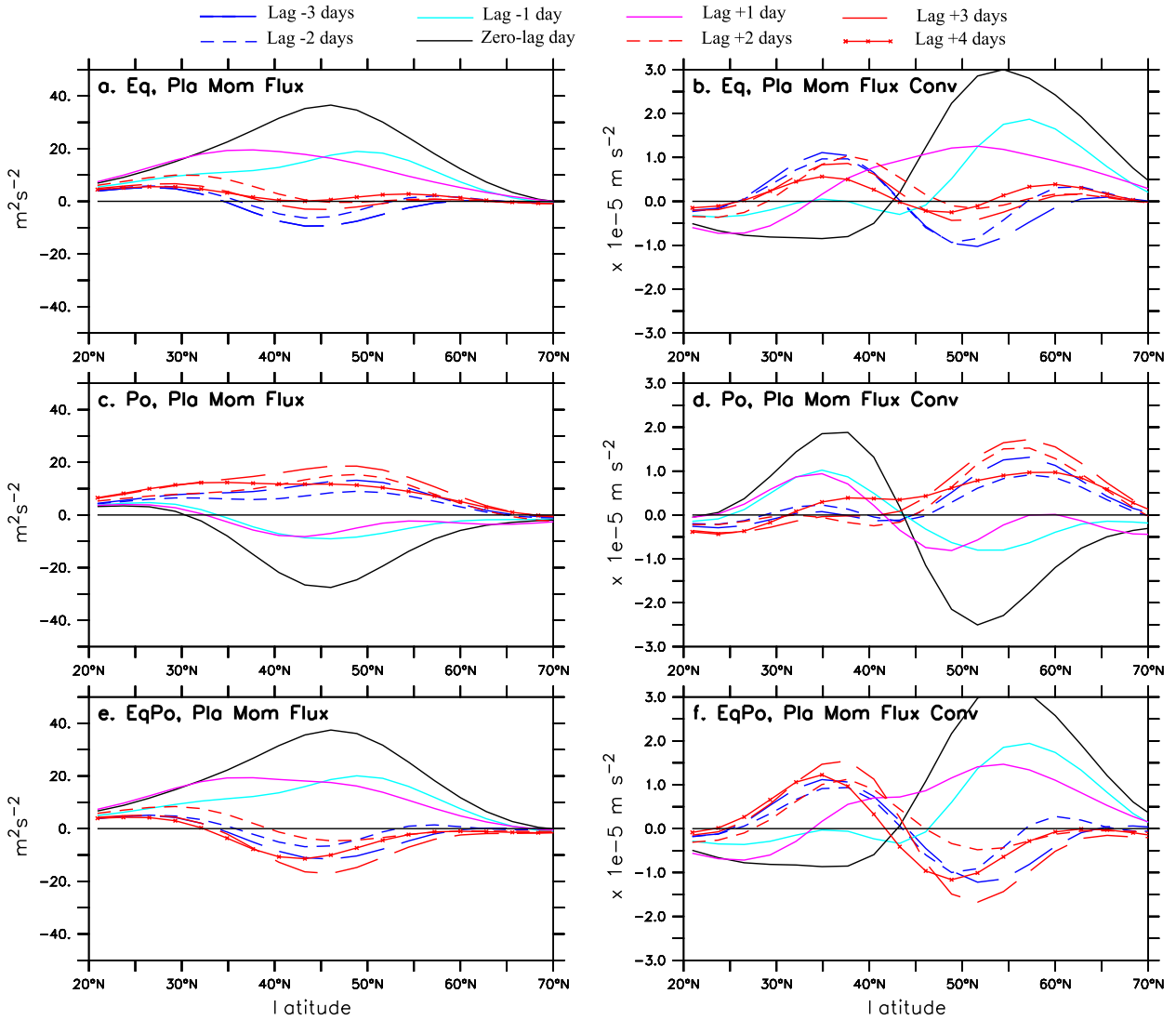


FIG. 10. Time lag composites of (a),(c),(d) the vertically averaged planetary wave momentum flux and (b),(d),(f) its convergence as a function of latitude: (a),(b) the planetary waves propagate equatorward (Eq composite); (c),(d) the planetary waves propagate poleward (Po composite); (e),(f) the planetary waves propagate equatorward and then poleward a few days later (EqPo composite). See text for more details on the computation of the Eq, Po, and EqPo composites.

On the contrary, a poleward-propagating wave tends to decelerate the jet.

The Po composite shows the reverse situation compared to the Eq composite. There is a deceleration of the jet from lag  $-1$  to lag  $+2$  days accompanied by a slight equatorward shift (Fig. 11c). The pulsing index decreases from 0 to  $-0.7$  and the shifting index from 0.2 to  $-0.4$  during that period (Fig. 11d). The two indices then increase to  $-0.1$  from lag  $+2$  to lag  $+5$  days. In that case, the two modes have roughly the same amplitude of variations.

An interesting result concerns the comparison between the variations of the indices for Eq and Po. For Po, the jet profile at the zero-lag day is recovered at lag  $+4$  days. This is not the case for Eq, where the jet is still much more

intense at lag  $+4$  days than at the zero-lag day. This is because, for Po, there is reflection of the waves on the poleward side of the jet around lag  $+2$  days (see Fig. 10c), which leads to a planetary wave forcing opposite to that occurring prior to lag  $+2$  days. On the contrary, the Eq composite does not show a reflection, which explains why the negative feedback at later lags is weak. The EqPo composite confirms this view. EqPo contains the subsample of Eq cases characterized by a reflection on the subtropical flank of the jet. For EqPo, there is a rapid decrease in both the pulsing and shifting indices between lag  $+2$  and lag  $+5$  days (Fig. 11f), while for Eq the decrease of these indices is small during the same time interval (Fig. 11b). The momentum flux convergence is

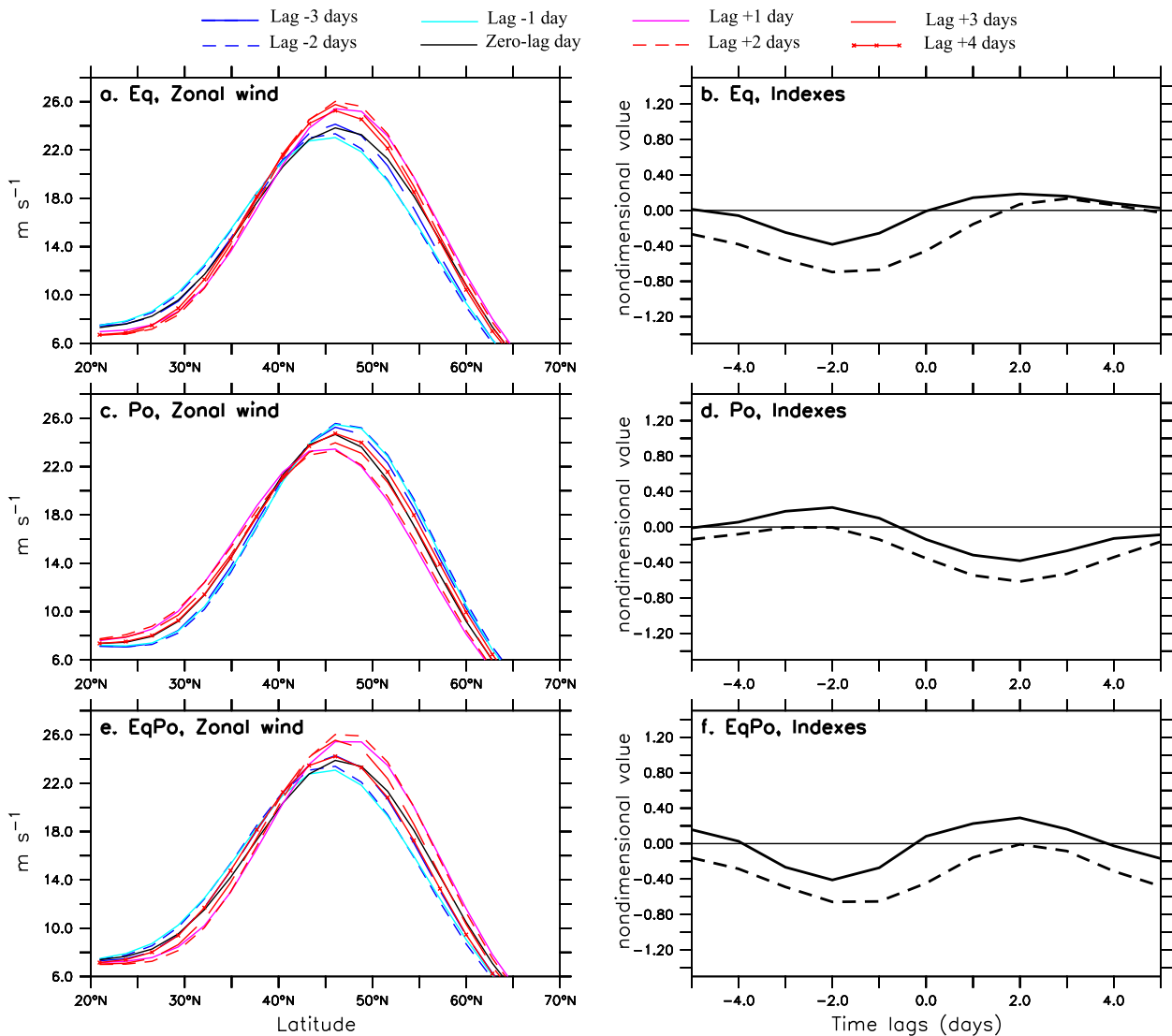


FIG. 11. (a),(c),(e) As in Figs. 10a, 10c, and 10e, respectively, but for the vertically averaged zonal-mean zonal wind. (b),(d),(f) The shifting (solid lines) and pulsing (dashed lines) indices for the same days as in (a), (c), and (e), respectively.

strongly negative in the latitudinal band 45°–55°N from lag +2 to lag +4 days for EqPo (Fig. 10f), while it is near zero for the same latitudes at the same time for Eq (Fig. 10b). Here again it is the reflection occurring on the subtropical side for EqPo cases that explains the negative planetary wave feedback on the jet variability.

## 5. Conclusions

The present paper is based on an analysis of nonlinear baroclinic wave life cycles and a long-term simulation performed with a quasigeostrophic model. It shows that the short-term planetary wave negative feedback acting on jet variability (Watterson 2002; Lorenz and Hartmann 2003; Simpson et al. 2014) can be attributed to wave

reflection. In this simple model, there are no tropical heating anomalies or topography that may excite planetary waves. Hence, these waves are triggered by baroclinic instability, similarly to synoptic waves.

Once developed, planetary waves tend to predominantly propagate equatorward because of spherical geometry (Simmons and Hoskins 1978; Orlandi 2003; Rivière 2009). A critical latitude is usually present on the subtropical flank of the jet, but as the waves propagate in that region they may interact nonlinearly with the jet and diminish the PV gradient there. This may potentially lead to the formation of a temporary turning latitude that will act to reflect the waves. Before the reflection, waves deposit their momentum on the jet core and on its poleward side, which acts to accelerate

the jet and displace it slightly poleward. After the reflection, waves deposit their momentum on the equatorward side of the jet and act to decelerate it in its core region. If there is absorption instead of reflection, the jet acceleration is amplified and persists much longer. In the long-term simulation, one-third of the equatorward-propagating waves tend to reflect, and two-thirds tend to be absorbed. These results confirm the observational study made by [Abatzoglou and Magnusdottir \(2006\)](#).

When planetary waves propagate poleward, they are reflected near the quasi-permanent turning latitude located on the poleward flank of the jet very close to its axis. Before the reflection, the jet is decelerated and shifted equatorward, whereas it is accelerated and shifted poleward after the reflection. Thus, planetary waves tend to suppress the jet variations that they drove a few days before. Because the waveguide is shifted equatorward relative to the jet core region, the planetary wave forcing and feedback act more efficiently on pulses of the jet intensity than on its latitudinal shifts. Indeed, an equatorward-propagating wave along such a waveguide tends to deposit momentum on the jet core and accelerate the jet. On the contrary, a poleward-propagating wave along the same waveguide tends to decelerate the jet.

The planetary waveguide effect underlined in the present study is nonlinear since it needs an important homogenization of the PV by waves breaking in the subtropical critical layer in order for reflection to occur. The PV homogenization is a necessary component for a turning latitude to appear on the equatorward flank of the jet, but this is often not enough. For instance, the decrease in phase speed is another ingredient that helps decreasing the refractive index to zero on the equatorward flank of the jet. In the normal-mode analysis, the decrease in phase speed was found to be more pronounced for planetary waves than synoptic waves. The explanation for such an observation is left for future studies. In the long-term simulation, it is easier to interpret the difference of behavior between planetary and synoptic waves. The jet acceleration and the homogenization of PV on its equatorward flank are triggered by both waves. Since planetary waves have lower phase speeds than synoptic waves, the critical layer of the former waves is more likely to be located south of the region of PV homogenization than that of the latter waves. This is the main reason why planetary waves are more inclined to reflect than synoptic waves.

The wavenumber at which the transition between reflecting and nonreflecting waves occurs can fluctuate from case to case. This is why the separation between planetary and synoptic waves differs between the normal-mode simulations and the long-term simulation. Indeed, the transition depends on the background flow

along which the waves propagate. The present study suggests that the structure of the time-mean momentum flux convergence helps separate the two kinds of behavior. Reflecting waves present two peaks in the time-mean momentum flux convergence on both sides of the jet, while nonreflecting waves exhibit only one peak.

The reflection of planetary waves detailed in the present study provides an interpretation of some results underlined in past studies. In particular, it explains the time variations of the cross-covariance between the principal component of the leading mode of jet variability and the planetary wave momentum forcing seen in many studies ([Lorenz and Hartmann 2001, 2003](#); [Simpson et al. 2014](#)). This cross-covariance usually gets a positive maximum 2 days before the peak in the principal component and a negative minimum 2 days after [see, e.g., Fig. 8a of [Lorenz and Hartmann \(2003\)](#), Fig. 5c of [Simpson et al. \(2014\)](#), or Fig. 9 of [Eichelberger and Hartmann \(2007\)](#)]. This corresponds to the typical time scale of the waveguide since the propagation from one side to another of the waveguide lasts roughly 2 days.

In future studies, both the short-term negative planetary eddy feedback and the more classical long-term positive synoptic eddy feedback (e.g., [Robinson 2000](#); [Zurita-Gotor et al. 2014](#)) should be taken into account to interpret midlatitude jet variability. In a companion paper ([Robert et al. 2016](#), manuscript submitted to *J. Atmos. Sci.*), we investigate both synoptic and planetary eddy feedbacks to interpret the emergence and persistence of the leading modes of jet variability in the same quasigeostrophic model. In particular, we show that synoptic waves also induce a short-term negative feedback—with a distinct mechanism—which mainly acts on jet pulses.

*Acknowledgments.* The authors would like to thank two anonymous reviewers for their useful comments, which helped to clarify the paper.

## APPENDIX

### Deriving the Refractive Index Formulation

The purpose of the appendix is to derive an expression for the refractive index in the three-level quasigeostrophic framework that takes into account the distinct Rossby radii of deformation. The analytical development is similar to the continuously stratified problem, which is first briefly recalled.

#### *a. The continuously stratified problem*

The classical Charney–Drazin problem investigates the vertical propagation of Rossby waves in a stratified

medium within the quasigeostrophic framework (Holton 1992). The potential vorticity is expressed in log-pressure coordinates as follows:

$$q = \nabla^2 \psi + f + \frac{f_0^2}{\rho_R} \frac{\partial}{\partial z^*} \left( \frac{\rho_R}{N^2} \frac{\partial \psi}{\partial z^*} \right), \quad (\text{A1})$$

where  $\rho_R = \rho_0 e^{-z^*/H}$  is the density profile of an isothermal atmosphere, and  $N$  is the Brunt–Väisälä frequency. We seek solutions of the linearized equation of conservation of potential vorticity of the form

$$\psi' = e^{z^*/(2H)} \text{Re}[\tilde{\psi}(y, z^*) e^{i(m\lambda - \omega t)}], \quad (\text{A2})$$

where  $\omega$  is the frequency. The factor  $e^{z^*/(2H)}$  is introduced to account for the decrease of density with height with a scale height  $H$ . It leads to the following expression (Matsumo 1970; Palmer 1982):

$$\frac{\partial^2 \tilde{\psi}}{\partial y^2} + \frac{f^2}{N^2} \frac{\partial^2 \tilde{\psi}}{\partial z^{*2}} + n^2 \tilde{\psi} = 0, \quad (\text{A3})$$

where

$$n^2 = \frac{\partial \bar{q} / \partial y}{\bar{u}_1 - c a \cos \varphi} - \frac{f^2}{4N^2 H^2} - \frac{m^2}{a^2 \cos^2 \varphi}. \quad (\text{A4})$$

We note that the second term on the rhs of Eq. (A4) appears because of the variation of  $\rho_R$  with altitude.

### b. The three-level problem

The expression of PV in the three levels written in Eqs. (2)–(4) can be thought of as being the result of the discretization of the continuous form of the quasigeostrophic PV in pressure coordinates:

$$\begin{aligned} q_1 &= f + \nabla^2 \psi_1 + f_0^2 \left[ \frac{\partial}{\partial p} \left( \frac{1}{\sigma} \frac{\partial \psi}{\partial p} \right) \right]_1 \\ &= f + \nabla^2 \psi_1 + R_0^{-2} (\psi_0 - \psi_1) - R_1^{-2} (\psi_1 - \psi_2), \end{aligned} \quad (\text{A5})$$

$$\begin{aligned} q_2 &= f + \nabla^2 \psi_1 + f_0^2 \left[ \frac{\partial}{\partial p} \left( \frac{1}{\sigma} \frac{\partial \psi}{\partial p} \right) \right]_2 \\ &= f + \nabla^2 \psi_2 + R_1^{-2} (\psi_1 - \psi_2) - R_2^{-2} (\psi_2 - \psi_3), \end{aligned} \quad (\text{A6})$$

and

$$\begin{aligned} q_3 &= f + \nabla^2 \psi_1 + f_0^2 \left[ \frac{\partial}{\partial p} \left( \frac{1}{\sigma} \frac{\partial \psi}{\partial p} \right) \right]_3 \\ &= f + \nabla^2 \psi_3 + R_2^{-2} (\psi_2 - \psi_3) - R_3^{-2} (\psi_3 - \psi_4), \end{aligned} \quad (\text{A7})$$

where  $\sigma$  is the stratification parameter, which varies with the pressure  $p$ . The streamfunction at levels above 1 and below 3 is represented by  $\psi_0 = \psi_1$  and  $\psi_4 = \psi_3$ ,

respectively. These equalities are closely related to the underlying rigid lid conditions of the model. Indeed, the vertical velocity being zero at the interfaces between levels 0 and 1 and between levels 3 and 4, this can be, in particular, satisfied by a zero temperature, which is equivalent to the vertical derivative of the streamfunction being zero. The Rossby radii of deformation between levels 0 and 1 and between levels 3 and 4 are represented by  $R_0$  and  $R_3$ , respectively.

To obtain the refractive index formulation for the three-level problem, we need to find a formulation for the linearized equation of the potential vorticity where double derivatives in  $y$  and  $p$  appear. Therefore, we follow the same approach as in the continuous problem by seeking wavelike solutions of the following form:

$$\begin{aligned} &(\psi'_0, \psi'_1, \psi'_2, \psi'_3, \psi'_4) \\ &= \left( \frac{R_1^2}{R_2^2} \tilde{\psi}_0, \frac{R_1}{R_2} \tilde{\psi}_1, \tilde{\psi}_2, \frac{R_2}{R_1} \tilde{\psi}_3, \frac{R_2^2}{R_1^2} \tilde{\psi}_4 \right) e^{i(m\lambda - \omega t)}, \end{aligned} \quad (\text{A8})$$

with the ratio  $R_1/R_2$  being introduced to account for the variation of the Rossby radius of deformation with height, similar to the treatment of density in Eq. (A2). By choosing  $R_0 = R_1^2/R_2$  and  $R_3 = R_2^2/R_1$  (i.e., a linear variation of the radius of deformation with pressure), the linearized PV can be expressed as

$$q'_1 = \frac{R_1}{R_2} \nabla^2 \tilde{\psi}_1 + \frac{1}{R_1^2} \left( \frac{\partial^2 \tilde{\psi}}{\partial p^2} \right)_1 - \frac{R_2}{R_1} \left( \frac{1}{R_1} - \frac{1}{R_2} \right)^2 \tilde{\psi}_1, \quad (\text{A9})$$

$$q'_2 = \nabla^2 \tilde{\psi}_2 + \frac{1}{R_1 R_2} \left( \frac{\partial^2 \tilde{\psi}}{\partial p^2} \right)_2 - \left( \frac{1}{R_1} - \frac{1}{R_2} \right)^2 \tilde{\psi}_2, \quad (\text{A10})$$

and

$$q'_3 = \frac{R_2}{R_1} \nabla^2 \tilde{\psi}_3 + \frac{1}{R_2^2} \left( \frac{\partial^2 \tilde{\psi}}{\partial p^2} \right)_3 - \frac{R_1}{R_2} \left( \frac{1}{R_1} - \frac{1}{R_2} \right)^2 \tilde{\psi}_3. \quad (\text{A11})$$

The linearized version of the conservation of PV [i.e., Eq. (1) without diabatic terms] can then be written at each level as

$$\frac{\partial^2 \tilde{\psi}_1}{\partial y^2} + \frac{R_2^2}{R_1^2} \frac{1}{R_1 R_2} \left( \frac{\partial^2 \tilde{\psi}}{\partial p^2} \right)_1 + n_1^2 \tilde{\psi}_1 = 0, \quad (\text{A12})$$

$$\frac{\partial^2 \tilde{\psi}_2}{\partial y^2} + \frac{1}{R_1 R_2} \left( \frac{\partial^2 \tilde{\psi}}{\partial p^2} \right)_2 + n_2^2 \tilde{\psi}_2 = 0, \quad \text{and} \quad (\text{A13})$$

$$\frac{\partial^2 \tilde{\psi}_3}{\partial y^2} + \frac{R_1^2}{R_2^2} \frac{1}{R_1 R_2} \left( \frac{\partial^2 \tilde{\psi}}{\partial p^2} \right)_3 + n_3^2 \tilde{\psi}_3 = 0, \quad (\text{A14})$$

where  $n_1^2$ ,  $n_2^2$ , and  $n_3^2$  are expressed in Eqs. (12), (13), and (14). The second terms on the rhs of the latter equations

are negative and are a function of the Rossby radii of deformation, consistent with the continuous problem [see Eq. (A4)]. We note that, when the two Rossby radii of deformation are equal ( $R_1 = R_2$ ), these terms are zero. Hence, when the two Rossby radii of deformation are different, the waves are less propagating.

## REFERENCES

- Abatzoglou, J. T., and G. Magnusdottir, 2004: Nonlinear planetary wave reflection in the troposphere. *Geophys. Res. Lett.*, **31**, L09101, doi:10.1029/2004GL019495.
- , and —, 2006: Opposing effects of reflective and non-reflective planetary wave breaking on the NAO. *J. Atmos. Sci.*, **63**, 3448–3457, doi:10.1175/JAS3809.1.
- Arakelian, A., and F. Codron, 2012: Southern Hemisphere jet variability in the IPSL GCM at varying resolutions. *J. Atmos. Sci.*, **69**, 3788–3799, doi:10.1175/JAS-D-12-0119.1.
- Balasubramanian, G., and S. Garner, 1997: The role of momentum fluxes in shaping the life cycle of a baroclinic wave. *J. Atmos. Sci.*, **54**, 510–533, doi:10.1175/1520-0469(1997)054<0510:TROMFI>2.0.CO;2.
- Barnes, E. A., and D. L. Hartmann, 2010: Testing a theory for the effect of latitude on the persistence of eddy-driven jets using CMIP3 simulations. *Geophys. Res. Lett.*, **37**, L15801, doi:10.1029/2010GL044144.
- , and —, 2011: Rossby wave scales, propagation, and the variability of eddy-driven jets. *J. Atmos. Sci.*, **68**, 2893–2908, doi:10.1175/JAS-D-11-039.1.
- , and L. M. Polvani, 2013: Response of the midlatitude jets, and of their variability, to increased greenhouse gases in the CMIP5 models. *J. Climate*, **26**, 7117–7135, doi:10.1175/JCLI-D-12-00536.1.
- Branstator, G., 2002: Circumglobal teleconnections, the jet stream waveguide, and the North Atlantic Oscillation. *J. Atmos. Sci.*, **15**, 1893–1910, doi:10.1175/1520-0442(2002)015<1893:CTTJSW>2.0.CO;2.
- Brunet, G., and P. H. Haynes, 1996: Low-latitude reflection of Rossby wave trains. *J. Atmos. Sci.*, **53**, 482–496, doi:10.1175/1520-0469(1996)053<0482:LLRORW>2.0.CO;2.
- Charney, J. G., and P. G. Drazin, 1961: Propagation of planetary-scale disturbances from the lower into the upper atmosphere. *J. Geophys. Res.*, **66**, 83–109, doi:10.1029/JZ066i001p00083.
- Eichelberger, S. J., and D. Hartmann, 2007: Zonal jet structure and the leading mode of variability. *J. Climate*, **20**, 5149–5150, doi:10.1175/JCLI4279.1.
- Feldstein, S., and S. Lee, 1998: Is the atmospheric zonal index driven by an eddy feedback? *J. Atmos. Sci.*, **55**, 3077–3086, doi:10.1175/1520-0469(1998)055<3077:ITAZID>2.0.CO;2.
- Gall, R., 1976: Structural changes of growing baroclinic waves. *J. Atmos. Sci.*, **33**, 374–390, doi:10.1175/1520-0469(1976)033<0374:SCGBW>2.0.CO;2.
- Geisler, J., and R. Dickinson, 1974: Numerical study of an interacting Rossby wave and barotropic zonal flow near a critical level. *J. Atmos. Sci.*, **31**, 946–955, doi:10.1175/1520-0469(1974)031<0946:NSOAIR>2.0.CO;2.
- Gerber, E., and G. Vallis, 2007: Eddy–zonal flow interactions and the persistence of the zonal index. *J. Atmos. Sci.*, **64**, 3296–3311, doi:10.1175/JAS4006.1.
- Held, I., 1983: Stationary and quasi-stationary eddies in the extratropical troposphere: Theory. *Large-Scale Dynamical Processes in the Atmosphere*, R. P. Pearce and B. J. Hoskins, Eds., Academic Press, 127–168.
- , and M. Suarez, 1994: A proposal for the intercomparison of the dynamical cores of atmospheric general circulation models. *Bull. Amer. Meteor. Soc.*, **75**, 1825–1830, doi:10.1175/1520-0477(1994)075<1825:APFTIO>2.0.CO;2.
- Holton, J., 1992: *An Introduction to Dynamic Meteorology*. 3rd ed. International Geophysics Series, Vol. 48, Academic Press, 511 pp.
- Hoskins, B. J., and T. Ambrizzi, 1993: Rossby wave propagation on a realistic longitudinally varying flow. *J. Atmos. Sci.*, **50**, 1661–1671, doi:10.1175/1520-0469(1993)050<1661:RWPOAR>2.0.CO;2.
- Karoly, D. J., 1983: Rossby wave propagation in a barotropic atmosphere. *Dyn. Atmos. Oceans*, **7**, 111–125, doi:10.1016/0377-0265(83)90013-1.
- Kidston, J., and E. P. Gerber, 2010: Intermodel variability of the poleward shift of the austral jet stream in the CMIP3 integrations linked to biases in 20th century climatology. *Geophys. Res. Lett.*, **37**, L09708, doi:10.1029/2010GL042873.
- Killworth, P., and M. E. McIntyre, 1985: Do Rossby-wave critical layers absorb, reflect, or over-reflect? *J. Fluid Mech.*, **161**, 449–492, doi:10.1017/S0022112085003019.
- Lorenz, D. J., 2014: Understanding midlatitude jet variability and change using Rossby wave chromatography: Wave–mean flow interaction. *J. Atmos. Sci.*, **71**, 3684–3705, doi:10.1175/JAS-D-13-0201.1.
- , and D. L. Hartmann, 2001: Eddy–zonal flow feedback in the Southern Hemisphere. *J. Atmos. Sci.*, **58**, 3312–3327, doi:10.1175/1520-0469(2001)058<3312:EZZFIT>2.0.CO;2.
- , and —, 2003: Eddy–zonal flow feedback in the Northern Hemisphere winter. *J. Climate*, **16**, 1212–1227, doi:10.1175/1520-0442(2003)16<1212:EFFFITN>2.0.CO;2.
- Magnusdottir, G., and P. H. Haynes, 1999: Reflection of planetary waves in three-dimensional tropospheric flows. *J. Atmos. Sci.*, **56**, 652–670, doi:10.1175/1520-0469(1999)056<0652:ROPWIT>2.0.CO;2.
- Marshall, J., and F. Molteni, 1993: Toward a dynamical understanding of planetary-scale flow regimes. *J. Atmos. Sci.*, **50**, 1792–1818, doi:10.1175/1520-0469(1993)050<1792:TADUOP>2.0.CO;2.
- Matsuno, T., 1970: Vertical propagation of stationary planetary waves in the winter Northern Hemisphere. *J. Atmos. Sci.*, **27**, 871–883, doi:10.1175/1520-0469(1970)027<0871:VPOSPW>2.0.CO;2.
- O’Rourke, A. K., and G. Vallis, 2013: Jet interaction and the influence of a minimum phase speed bound on the propagation of eddies. *J. Atmos. Sci.*, **70**, 2614–2628, doi:10.1175/JAS-D-12-0303.1.
- Orlanski, I., 2003: Bifurcation in eddy life cycles: Implication for storm-track variability. *J. Atmos. Sci.*, **60**, 993–1023, doi:10.1175/1520-0469(2003)60<993:BIELCI>2.0.CO;2.
- Palmer, T., 1982: Properties of the Eliassen–Palm flux for planetary scale motions. *J. Atmos. Sci.*, **39**, 992–997, doi:10.1175/1520-0469(1982)039<0992:POTEPF>2.0.CO;2.
- Rivière, G., 2009: Effect of latitudinal variations in low-level baroclinicity on eddy life cycles and upper-tropospheric wave-breaking processes. *J. Atmos. Sci.*, **66**, 1569–1592, doi:10.1175/2008JAS2919.1.
- Robinson, W., 1996: Does eddy feedback sustain variability in the zonal index? *J. Atmos. Sci.*, **53**, 3556–3569, doi:10.1175/1520-0469(1996)053<3556:DEFSVI>2.0.CO;2.
- , 2000: A baroclinic mechanism for the eddy feedback on the zonal index. *J. Atmos. Sci.*, **57**, 415–422, doi:10.1175/1520-0469(2000)057<0415:ABMFTE>2.0.CO;2.

- , 2006: On the self-maintenance of midlatitude jets. *J. Atmos. Sci.*, **63**, 2109–2122, doi:[10.1175/JAS3732.1](https://doi.org/10.1175/JAS3732.1).
- Simmons, A. J., and B. J. Hoskins, 1978: The life cycles of some nonlinear baroclinic waves. *J. Atmos. Sci.*, **35**, 414–432, doi:[10.1175/1520-0469\(1978\)035<0414:TLCOSN>2.0.CO;2](https://doi.org/10.1175/1520-0469(1978)035<0414:TLCOSN>2.0.CO;2).
- Simpson, I., T. Shepherd, P. Hitchcock, and J. F. Scinocca, 2014: Southern annular mode dynamics in observations and models. Part II: Eddy feedbacks. *J. Atmos. Sci.*, **71**, 2489–2515, doi:[10.1175/JAS-D-13-0325.1](https://doi.org/10.1175/JAS-D-13-0325.1).
- Thompson, D. W. J., and J. M. Wallace, 2000: Annular modes in the extratropical circulation. Part I: Month-to-month variability. *J. Climate*, **13**, 1000–1016, doi:[10.1175/1520-0442\(2000\)013<1000:AMITEC>2.0.CO;2](https://doi.org/10.1175/1520-0442(2000)013<1000:AMITEC>2.0.CO;2).
- Vallis, G., Ed., 2006: *Atmospheric and Oceanic Fluid Dynamics: Fundamentals and Large-Scale Circulation*. Cambridge University Press, 745 pp.
- Watterson, I., 2002: Wave–mean flow feedback and the persistence of simulated zonal flow vacillation. *J. Atmos. Sci.*, **59**, 1274–1288, doi:[10.1175/1520-0469\(2002\)059<1274:WMFFAT>2.0.CO;2](https://doi.org/10.1175/1520-0469(2002)059<1274:WMFFAT>2.0.CO;2).
- Yu, J.-Y., and D. L. Hartmann, 1993: Zonal flow vacillation and eddy forcing in a simple GCM of the atmosphere. *J. Atmos. Sci.*, **50**, 3244–3259, doi:[10.1175/1520-0469\(1993\)050<3244:ZFVAEF>2.0.CO;2](https://doi.org/10.1175/1520-0469(1993)050<3244:ZFVAEF>2.0.CO;2).
- Zhang, Y., X.-Q. Yang, Y. Nie, and G. Chen, 2012: Annular mode–like variation in a multilayer quasigeostrophic model. *J. Atmos. Sci.*, **69**, 2940–2958, doi:[10.1175/JAS-D-11-0214.1](https://doi.org/10.1175/JAS-D-11-0214.1).
- Zurita-Gotor, P., J. Blanco-Fuentes, and E. Gerber, 2014: The impact of baroclinic eddy feedback on the persistence of jet variability in the two-layer model. *J. Atmos. Sci.*, **71**, 410–429, doi:[10.1175/JAS-D-13-0102.1](https://doi.org/10.1175/JAS-D-13-0102.1).